



1 **Buoyant calving and ice-contact lake evolution at Pasterze Glacier (Austria) in the period**

2 **1998-2019**

3

4

5 Andreas Kellerer-Pirklbauer (1), Michael Avian (2), Douglas I. Benn (3), Felix Bernsteiner (1),

6 Philipp Krisch (1), Christian Ziesler (1)

7

8 (1) Cascade - The mountain processes and mountain hazards group, Institute of Geography and

9 Regional Science, University of Graz, Austria

10 (2) Department of Earth Observation, Zentralanstalt für Meteorologie und Geodynamik

11 (ZAMG), Vienna, Austria

12 (3) School of Geography and Geosciences, University of St Andrews, St Andrews, UK

13

14 **Correspondence**

15 Andreas Kellerer-Pirklbauer; andreas.kellerer@uni-graz.at

16

17 **Funding information**

18 Research relevant for this study was funded through different projects: (a)

19 Austrian Science Fund, project no. FWF P18304-N10, (b) Hohe Tauern National Park authority

20 (various projects), (c) Glockner Ökofonds (GROHAG) 2018, and (d) Austrian Alpine Association

21 (through the annual glacier monitoring program)

22



23 **Abstract:** Rapid growth of proglacial lakes in the current warming climate can pose significant
24 outburst flood hazards, increase rates of ice mass loss, and alter the dynamic state of glaciers.
25 We studied the nature and rate of proglacial lake evolution at Pasterze Glacier (Austria) in the
26 period 1998-2019 using different remote sensing (photogrammetry, laserscanning) and
27 fieldwork-based (GPS, time-lapse photography, geoelectrical resistivity tomography/ERT, and
28 bathymetry) data. Glacier thinning below the spillway level and glacier recession caused
29 flooding of the glacier, initially forming a glacier-lateral to supraglacial lake with subaerial and
30 subaquatic debris-covered dead-ice bodies. The observed lake size increase in 1998-2019
31 followed an exponential curve (1998: 1900 m²; 2019: 304,000 m²). ERT data from 2015 to 2019
32 revealed widespread existence of massive dead-ice bodies exceeding 25 m in thickness near the
33 lake shore. Several large-scale and rapidly occurring buoyant calving events were detected in
34 the 48 m deep basin by time-lapse photography, indicating that buoyant calving is a crucial
35 process for fast lake expansion. We identified a sequence of processes: glacier recession into a
36 basin and glacier thinning below spillway-level; glacio-fluvial sedimentation in the glacial-
37 proglacial transition zone covering dead ice; initial formation and accelerating enlargement of a
38 glacier-lateral to supraglacial lake by ablation of glacier ice and debris-covered dead ice forming
39 thermokarst features; increase in hydrostatic disequilibrium leading to destabilization of ice at
40 the lake bottom or at the near-shore causing fracturing, tilting, disintegration or emergence of
41 new icebergs due to buoyant calving; and gradual melting of icebergs along with iceberg
42 capsizing events. We conclude that buoyant calving, previously not reported from the European
43 Alps, might play an important role at alpine glaciers in the future as many glaciers are expected
44 to recede into valley or cirque overdeepenings.



45

46 **Keywords:** ice-contact lake; dead ice decay; buoyant calving; hydrostatic equilibrium; proglacial
47 landscape evolution

48

49 1. INTRODUCTION

50 Ongoing recession of mountain glaciers worldwide reveals dynamic landscapes exposed to high
51 rates of geomorphological and hydrological changes (Carrivick and Heckmann, 2017). In suitable
52 topographic conditions, proglacial lakes may form, including ice-contact lakes (physically
53 attached to an ice margin) and ice-marginal lakes (lakes detached from or immediately beyond
54 a contemporary ice margin) (Benn and Evans, 2010; Carrivick and Tweed, 2013). Such lakes
55 have increased in number, size and volume around the world due to climate warming-induced
56 glacier melt (Carrivick and Tweed, 2013; Otto, 2019). Buckel et al. (2018) for instance studied
57 the formation and distribution of proglacial lakes since the Little Ice Age (LIA) in Austria
58 revealing a continuous acceleration in the number of glacier-related lakes particularly since the
59 turn of the 21st century.

60

61 The formation of proglacial lakes is important because they can pose significant outburst flood
62 hazards (e.g. Richardson and Reynolds, 2000; Harrison et al., 2018), increase rates of ice mass
63 loss, and alter the dynamic state of glaciers (e.g. Kirkbride and Warren, 1999; King et al., 2018,
64 2019; Liu et al., 2020). However, detailed descriptions of proglacial lake formation and related
65 subaerial and subaquatic processes are still rare. Carrivick and Heckmann (2017) pointed out



66 that there is an urgent need for inventories of proglacial systems including lakes to form a
67 baseline from which changes could be detected.
68
69 The evolution of proglacial lakes is commonly linked to the subsurface, particularly to changes
70 in the distribution of debris-covered dead ice (defined here as any part of a glacier which has
71 ceased to flow) and permafrost-related ground ice bodies (Bosson et al., 2015; Gärtner-Roer
72 and Bast, 2019) affecting lake geometry and areal expansion.
73
74 Water bodies at the glacier surface form initially as supraglacial lakes which might be either
75 perched lakes (i.e. above the hydrological base level of the glacier) or base-level lakes (spillway
76 controlled). The former type is prone to drainage if the perched lake connects to the englacial
77 conduit system (Benn et al., 2001). Rapid areal expansion of such lakes is controlled by
78 waterline and subaerial melting of exposed ice cliffs and calving (Benn et al., 2001).
79 Furthermore, supraglacial lakes may transform into proglacial lakes lacking any ice core (full-
80 depth lakes) through melting of lake-bottom ice. However, this is a slow process in which
81 energy is conducted from the overlying water and cannot account for some observed instances
82 of fast lake-bottom lowering ($>10 \text{ m yr}^{-1}$). It has been argued that fast lake-bottom lowering
83 could occur by buoyant calving (Dykes et al., 2010; Thompson et al., 2012), but the rare and
84 episodic nature of such events mean that little is known about how buoyant calving might
85 contribute to the transformation of supraglacial lakes into full-depth lakes.
86



87 Ablation of lake-terminating glaciers may lead to the development of submerged ice feet or
88 thinning of ice margins below the point of hydrostatic equilibrium. Rises in lake level can have
89 similar results. In such cases, ice becomes super-buoyant and subject to net upward buoyant
90 forces, promoting fracture propagation and calving (Benn et al., 2007). Calving by this process
91 has been described by Holdsworth (1973), Warren et al. (2001) and Boyce et al. (2007).

92 Hydrostatic disequilibrium caused the sudden disintegration of debris-covered dead ice in the
93 proglacial area of Pasterze Glacier in September 2016 (Fig. 2). This event was briefly described
94 in Kellerer-Pirklbauer et al. (2017) and was one of the main motivations for the present study.

95

96 In the present study, we analysed rates and processes of glacier recession and formation and
97 evolution of an ice-contact lake at Pasterze Glacier, Austria, over a period of 22 years. The aims
98 of this study are (i) to examine glaciological and morphological changes at the highly dynamic
99 glacial-proglacial transition zone of the receding Pasterze Glacier and (ii) to discuss related
100 processes which formed the proglacial lake named Pasterzensee (*See* is German for lake) during
101 the period 1998-2019. Regarding the latter, we focus particularly on the significance of buoyant
102 calving. In doing so, we consider subaerial, subsurface, aquatic, as well as subaquatic domains
103 applying fieldwork-based and remote-sensing techniques.

104

105 **2. STUDY AREA**

106 The study area comprises the glacial-proglacial transition zone of Pasterze Glacier, Austria. This
107 glacier covered 26.5 km² during the LIA maximum around 1850 and is currently the largest
108 glacier in the Austrian Alps with an area of 15.4 km² in 2019 (Fig. 1). The glacier is located in the



109 Glockner Mountains, Hohe Tauern Range, at 47°05'N and 12°43'E (Fig. 1b). The gently sloping,
110 4.5 km long glacier tongue is connected to the upper part of the glacier by an icefall named
111 Hufeisenbruch (meaning "horseshoe icefall" in German) attributed to its former shape in plan
112 view. This icefall disintegrated and narrowed substantially during the last decades attributed to
113 the decrease of ice replenishment from the upper to the lower part of the glacier (Kellerer-
114 Pirklbauer, et al. 2008; Kaufmann et al., 2015).

115

116 The longest time series of length changes at Austrian glaciers has been compiled for Pasterze
117 Glacier. Measurements at this glacier were initiated in 1879 and interrupted in only three years.
118 Furthermore, annual glacier flow velocity measurements and surface elevation changes at
119 cross-sections were initiated in the 1920s with almost continuous measurements since then
120 (Wakonigg and Lieb, 1996). Technical details of the measurement can be found in Kellerer-
121 Pirklbauer et al. (2008) as well as in Lieb and Kellerer-Pirklbauer (2018). Minor glacier advances
122 at Pasterze Glacier occurred in only seven years since 1879, the most recent of which was in the
123 1930s. Even during wetter and cooler periods (1890s, 1920s and 1965-1980), the glacier did not
124 advance substantially, which can be attributed to the long response time of the glacier (Zuo and
125 Oerlemans, 1997). In 1959-2019, Pasterze Glacier receded by 1550 m, three times the mean
126 value for all Austrian glaciers (520 m), related to its large size. Today, Pasterze Glacier is
127 characterised by annual mean recession rates in the order of 40 m yr⁻¹ (Lieb and Kellerer-
128 Pirklbauer, 2018) causing a rather high pace of glacial to proglacial landscape modification
129 favouring paraglacial response processes (Ballantyne, 2002; Avian et al., 2018).

130



131 Analyses of brittle and ductile structures at the surface of the glacier tongue revealed that
132 many of these structures are relict and independent from current glacier motion (Kellerer-
133 Pirklbauer and Kulmer, 2019). The glacier tongue is in a state of rapid decay and thinning and
134 thus prone to fracturing by normal fault formation. Englacial and subglacial melting of glacier
135 ice caused the formation of circular collapse structures with concentric crevasses, which form
136 when the ice between the glacier surface and the roof of water channels decreases. Kellerer-
137 Pirklbauer and Kulmer (2019) concluded that the tongue of the Pasterze Glacier is currently
138 turning into a large dead-ice body characterized by a strong decrease in ice replenishment from
139 further up-glacier, movement cessation, accelerated thinning and ice disintegration by supra-,
140 en- and subglacial ablation, allowing normal fractures and circular collapse features to develop.
141 This rapid deglaciation and decrease in activity are favourable for dead ice and proglacial lake
142 formation.

143

144 An automatic weather station is located close to the study area operated by Austrian Hydro
145 Powers since 1982 (AWS in Fig. 1a). The coldest year in the period 1998-2019 was 2005 with a
146 mean annual air temperature (MAAT) of 0.9°C whereas the warmest year was 2015 with 4.0°C
147 (range 3.1°C, mean of the 22-year period 2.4°C; Fig. 1c). Interannual variation is high although a
148 warming trend is clear. A MAAT value >3°C was calculated for eight of the nine years between
149 2011 and 2019. No such high MAAT values were recorded for the entire previous 28-year
150 period 1982-2010 indicating significant recent atmospheric warming. Two ground temperature
151 monitoring sites were installed near the lake in fluvio-glacial sediments in 2018 (PRO1 – one
152 sensor at the surface; PRO2 – three sensors at the surface and at 10 and 40 cm depths; location



153 see Fig. 1a) using GeoPrecision data logger equipped with PT1000 temperature sensors
154 (accuracy of $\pm 0.05^{\circ}\text{C}$) and logging hourly. Positive mean values for a 363-day long period
155 (13.09.2018-10.09.2019) were recorded for both sites (PRO1: 2.6°C , PRO2: $3.7\text{-}3.9^{\circ}\text{C}$) suggesting
156 permafrost-free conditions in the proglacial area and unfavourable conditions for long-term
157 dead ice conservation even below a protecting sediment cover.

158

159 **3. MATERIAL AND METHODS**

160 **3.1. GNSS data**

161 The terminus position of Pasterze Glacier was measured directly in the field by Global
162 Navigation Satellite System (GNSS) techniques in 14 years between 2003 and 2019 (annually
163 between 2003 and 2005, in 2008, and between 2010 and 2019). Direct measurements of the
164 subaerial glacier limit are essential in areas where debris cover obscures the glacier margin,
165 hindering the successful application of remote-sensing techniques (e.g. Kaufmann et al., 2015;
166 Avian et al., 2020). GNSS measurements were mostly carried out in September of the above
167 listed years, thus, close to the end of the glaciological years of mid-latitude mountain regions.
168 Until 2013, conventional GPS technique was applied using different handheld GARMIN devices
169 (geometric accuracy in the range of meters). Afterwards, real time kinematics (RTK) technique
170 was used, where correction data from the base station whose location is precisely known are
171 transmitted to the rover (geometric accuracy in the range of centimetres). We utilized a
172 TOPCON HiPer V Differential GPS (DGPS) system. The base station was either our own local
173 station (base-and-rover setup) or we obtained correction signals from a national correction-
174 data provider (EPOSA, Vienna).



175

176 **3.2. Airborne photogrammetry and land cover classification**

177 Nine sets of high-resolution optical images with a geometric resolution of 0.09-0.50 m derived
178 from aerial surveys between 1998 and 2019 (Table 1) were available for land cover analyses.
179 For the years 2003, 2006, and 2009, the planimetric accuracy of single point measurements is
180 better than ± 20 cm (Kaufmann et al., 2015). Comparable planimetric accuracies can be
181 expected for the other stages. The optical data sets were used for visual classification using a
182 hierarchical interpretation key following a scheme developed for Pasterze Glacier by Avian et al.
183 (2018) for laserscanning data and modified later for optical data by Krisch and Kellerer-
184 Pirklbauer (2019). Land cover classification was accomplished at a scale of 1:300 (for the stages
185 1998-2015; data based on Krisch and Kellerer-Pirklbauer, 2019) or 1:200 (2018-2019; this
186 study). The classification results for a 1.77 km² area at Pasterze Glacier were published earlier
187 by Krisch and Kellerer-Pirklbauer (2019) for 1998, 2003, 2006, 2009, 2012, and 2015. For a 0.37
188 km² area, manual land cover classification was accomplished in this study for 2018 and 2019
189 using the same mapping key.

190

191 **3.3. Terrestrial laserscanning**

192 The glacial-proglacial transition zone of Pasterze Glacier has been monitored by terrestrial laser
193 scanning (TLS) since 2001 from the scanning position Franz-Josefs-Höhe (FJH). The area of
194 interest in the scan sector covers 1.2 km² (Fig. 1a). Using scanning position FJH, one minor
195 limitation of TLS-based data for glacier lake delineation is the oblique scan geometry causing
196 data gaps due to scan-shadowed areas (Avian et al., 2018; 2020). Until 2009 the Riegli LPM-2k



197 system was used followed by the Riegl LMS-Z620 system since then. Technical specifications
198 regarding the two Riegl laser scanning systems as well as the configuration of the geodetic
199 network (scanning position and reference points) can be found in Avian et al. (2007; 2018).
200 Processing and registration of the TLS data was performed in Riegl RiScan, subsequently DTMs
201 (with 1 or 0.5 m grid resolution) were calculated in Golden Software Surfer. In this study we
202 used the DTMs to delineate the water bodies in the scan sector manually (for details see Avian
203 et al., 2020) supported by GPS data (cf. above) for the glacier boundary. TLS-data from 2010 to
204 2017 (13.09.2010, 27.09.2011, 07.09.2012, 24.08.2013, 09.09.2014, 12.09.2015, 27.08.2016,
205 and 22.09.2017) were used.

206

207 **3.4. Time-lapse photography**

208 At Pasterze Glacier six remote digital cameras (RDC) are installed to monitor mainly
209 glaciological processes with a very high temporal resolution (see Avian et al., 2020; overview
210 regarding the six cameras). One time-lapse camera was operated by the Grossglockner
211 Hochalpenstraße AG (GROHAG) using a Panomax system. The model used is a Roundshot
212 Livecam Generation 2 (Seitz, Switzerland) with a recording rate of mostly 5 minutes during
213 daylight. The camera is installed at the Franz-Josefs-Höhe lookout point (Fig. 1a) at an elevation
214 of 2380 m asl and, thus, 310 m above the present lake level of Lake Pasterzensee. Based on this
215 optical data, Kellerer-Pirklbauer et al. (2017) reported a sudden ice-disintegration event at the
216 glacier lake in September 2016 where tilting, lateral shifting, and subsidence of the ground
217 accompanied by complete ice disintegration of a debris-covered ice body occurred. For this
218 study, we visually checked all available Panomax images from 2016 to 2019. Four large-scale



219 and rapidly occurring ice-breakup events (IBE) were detected in the period September 2016 to
220 October 2019 (IBE1: 20.09.2016; IBE2: 09.08.2018, IBE3: 26.09.2018, IBE4: 24.10.2018). The
221 effects on the proglacial landscape during these four IBE was quantitatively analysed as follows.
222

223 For the orthorectification process of the Panomax images (7030x2048 px) it is necessary to find
224 a suitable mathematical model. To get the necessary parameters for this model, control points
225 are needed which are visible in both the Panomax images and pre-existing orthophotos used
226 for the orthorectification process. We applied an interpolation approach using the rubber
227 sheeting model in ERDAS IMAGINE 2018. This model calculates a Triangulated Irregular
228 Network (TIN) for all control points at the reference orthophoto and at the Panomax image and
229 transforms the calculated triangles of the oblique images in such a way that they equal the ones
230 of the reference orthophoto. First degree polynomials were used for the transformation within
231 the triangles. Only control points at the lake level were utilized to achieve a maximum accuracy
232 at lake-level objects. Reasons for minor geometric errors in the analysed orthorectified images
233 were changes in the lake level or an offset of the camera (maximum of 5 px). Direct lake level
234 measurements at Lake Pasterzensee between 25.06.2019 and 12.09.2019 indicate an
235 amplitude of 95 cm (temperature range 0.9-1.8°C) in the 80-day period (pers. comm. Jakob
236 Abermann), thus, we assume a lake level variation in the order of 1m during the summer
237 months. Three groups of control points were generated using the three pre-existing
238 orthophotos of 11.07.2015, 11.09.2018, and 15.11.2018 (Table 1) and suitable Panomax images
239 from the same days. For the IBE1 we used the model of 11.07.2015, for IBE2 and IBE3 the
240 model of 11.09.2018, and for IBE 4 the one of 15.11.2018. The calculated orthorectified images



241 have a geometric resolution of 0.2 m. ArcGIS 10.5 was subsequently used to analyse landform
242 changes. For more details see Bernsteiner (2019).

243

244 **3.5. Geophysics**

245 Electrical resistivity tomography (ERT) and seismic refraction (SR) has been applied in the study
246 area between 2015 and 2019. For space reasons, we focus only on selected aspects of the ERT
247 results in this paper. Electrical resistivity is a physical parameter related to the chemical
248 composition of a material and its porosity, temperature, water and ice content (Kneisel and
249 Hauck 2008). For ERT a multi-electrode system (GeoTom, Geolog, Germany) and two-
250 dimensional data inversion (Res2Dinv) was applied. ERT was carried out at a total of 43 profiles
251 (3 in 2015, 4 in 2016, 4 in 2017 [Fig. 3a,b], 5 in 2018, and 27 in 2019 [Fig. 3c]) with 2 or 4 m
252 electrode spacing and profile lengths of 80-196 m. Salt water was sometimes used at the
253 electrodes to improve electrical contact. RTK was applied to measure the position of each
254 electrode and thus the course of the profile (Fig. 3b). We applied in most cases both the
255 Wenner and Schlumberger arrays (Kneisel and Hauck, 2008). Focus is given here on the Wenner
256 results, which are more suitable for layered structures (Kneisel and Hauck 2008). ERT data from
257 2015 and 2016 were taken from Hirschmann (2017) and Seier et al. (2017). The apparent
258 resistivity data were inverted in Res2Dinv using the robust inversion modelling. Bad datum
259 points were removed before the inversion. The number of iterations was stopped when the
260 change in the RMS error between two iterations was small (Locke, 2000).

261

262 **3.6. Bathymetry**



263 Sonar measurements were carried out at Lake Pasterzensee at the 13.09.2019. Water depth in
264 the lake was measured with a Deeper Smart Sonar CHIRP+ system (depth range 0.15-100 m)
265 consisting of an echo sounding device and a GPS positioning sensor. The estimated accuracy of
266 raw water-depth measurements should be less than 10 cm according to the manufacturer. The
267 system was mounted on a Styrofoam platform for stability reasons and dragged behind a small
268 (and rather unstable) inflatable canoe operated by two people. Altogether 4276 water depth
269 measurements along a 4.3 km long route were accomplished (Fig. 1d) measuring with 290 kHz
270 (cone angle 16°). Because icebergs and wind cause boat instability, the canoe was not navigated
271 along a regular shore-to-shore route but rather in a zigzag mode starting in the northwest of
272 the lake and ending in the southeast. GPS and water depth data were imported into ArcGIS for
273 further analysis. To compute the lake geometry, the measured lake depth values and a lake
274 mask of September 2019 were combined using the Topo to Raster interpolation tool to
275 calculate a digital terrain model (DTM) with a 5m grid resolution. Lake volume was calculated
276 using the functional surface toolset.

277

278 **4. RESULTS**

279 **4.1. Glacier recession and areal expansion of the lake**

280 Figure 4a depicts the terminus positions between 1998 and 2019 as well as the proglacial water
281 surfaces including Lake Pasterzensee and the proglacial basin as defined for September 2019
282 (area of 0.365 km²). The glacier steadily receded into the current proglacial basin over a
283 longitudinal distance of c.1.4 km. In detail, however, this recession was not evenly distributed
284 along the glacier margin due to differential ablation below the uneven supraglacial debris. The



285 east part of the glacier tongue receded up-valley beyond the proglacial basin. The west part of
286 the glacier tongue is still in contact with the proglacial lake and changed morphologically rather
287 little during the last two decades. Figure 4a also depicts 100 m wide strips where mean values
288 for longitudinal and lateral backwasting were calculated. Results are shown in Fig. 4b. The
289 longitudinal backwasting rate was between 29.0 and 217.2 m yr⁻¹, 2 to 19 times larger than the
290 lateral backwasting rate of 7.3 to 13.2 m yr⁻¹. High annual longitudinal backwasting rates were
291 measured in most years when the glacier was in the basin. Since 2017, this rate drastically
292 dropped, presumably due to the detachment of the glacier from the lake.

293

294 Figure 5 illustrates glacier recession and the evolution of proglacial water bodies for the period
295 1998-2019 in relation to the 0.365 km² proglacial basin as defined for September 2019. In 1998
296 only 0.5% of the basin was covered by water (Fig. 5a). Up to 2006, water surfaces still covered
297 less than 5% of the basin (Fig. 5c). By 2009, this value increased to 11.2% (Fig. 5d) and was
298 rather constant until two years later (Fig. 5f). By 2016, more than 50% of the basin was covered
299 by water (Fig. 5k) and in 2019 water surfaces in the basin covered 83.2% (Fig. 5n). The increase
300 in water surface areas in the basin since 1998 follows an exponential curve (Fig. 6a). However,
301 in single years this areal increase follows a distinct pattern with enlargement of water surfaces
302 during summer and a decrease in autumn due to lake level lowering as revealed by field
303 observations. The exceptionally low value of November 2018 (62.4%) in relation to September
304 2018 (73.2%) is related to the widespread existence of ice floes. Figure 6a also depicts the
305 extent of icebergs in the proglacial basin with values below 1% in most cases. High percentage



306 values were only mapped for 15.11.2018 (7.3%) suggesting rapid iceberg loss during the
307 ablation season 2019.

308

309 **4.2. Land cover change in the lake-proximal surrounding since 1998**

310 Different glacial and proglacial surface types and landforms were mapped for a 0.76 km² area in
311 the glacial-proglacial transition zone for nine different stages between 1998 and 2019 (Fig. 7).

312 The visual landform classification gives a more detailed picture on landform changes in the area
313 of interest. Figure 6b quantitatively summarises the relative changes of different surface types

314 in this transition zone. Debris-poor, rather clean-ice covered 58% of the area in 1998, decreased
315 to 9.3% until 2015, and vanished afterwards from the area. In contrast, debris-rich glacier parts

316 covered in all nine stages between 20.5% (2019) and 33.4% (2015) of the transition zone. For
317 this class, areal losses due to glacier recession were partly compensated by areal gains due to

318 an increase in supraglacial debris-covered areas. Water surfaces increased from 2.1% in 1998 to
319 45.5% in 2019. The low value for 15.11.2018 is related to ice floes (3.4%), data gaps (4.1%), as

320 well as high values for both debris-rich (2.1%) and debris-poor (1.5%) icebergs. Areas covered
321 by bedrock and vegetation were always around 4%. Areas covered by fine-grained sediments

322 reached a maximum in 2012 decreasing substantially afterwards (mainly due to lake extension).

323 Areas covered by coarse-grained sediments increased from 3.3% in 1998 to about 26-27% in

324 2018 and 2019 and are located at the northern and eastern margin of the basin. Finally, dead

325 ice holes were mapped for all stages, but their spatial extent was always very small (maximum

326 in 2012 with a total area of 618 m²) and covered less than 0.1% of the basin.

327



328 **4.3. Buoyant calving at the ice-contact lake**

329 Four large-scale ice-breakup events (IBE) related to buoyancy were detected for the period
330 September 2016 to October 2019 (IBE1: 20.09.2016; IBE2: 09.08.2018, IBE3: 26.09.2018, and
331 IBE4: 24.10.2018). Twelve smaller to mid-sized iceberg-tilting or capsize events were
332 additionally documented by the Panomax images (27.05.2017, 28.05.2017, 09.06.2017,
333 11.06.2017, 20.06.2017, 05.07.2017, 19.07.2017, 25.09.2017, 22.06.2018, 23.09.2018,
334 26.09.2018, and 30.10.2018).

335

336 IBE1 occurred on 20.09.2016. Figure 8a presents two ortho-images from this event at its
337 beginning (9:00 am) and its end (11:15 am). The latter also indicates the position of the
338 geoelectric profile ERT17-1 for orientation. Figure 2 visualizes the same event. Different
339 processes occurred as indicated by the capital letters in Fig. 7a: Limnic transgression (A and F)
340 of water due to tilting of ice slabs, uplift of a debris-covered ice slab (B and G), formation of a
341 massive crevasse (C), complete ice disintegration (D), ice disintegration and lateral
342 displacement of several ice slabs (E), and drying out of a meltwater channel (H). All processes
343 apart from the limnic transgressions ended by 11:15 am, the latter terminated at 3:30 pm. The
344 formation of the large crevasse started initially at 9:30 am, followed by a rapid widening until
345 9:45 am (crack width 3.5 m), steady conditions until 10:45 am, followed by a second widening
346 phase (crack width 5.5 m) until 10:50 am (see inset graph in Fig. 8a). The morphologically most
347 distinct event happened between 9:50 am (Fig. 2d) and 9:55 am (Fig. 2e) when the total
348 collapse of a 1700 m² large ice slab occurred accompanied by lateral shift and tilting of



349 neighbouring ice slabs by lateral push (E) and lowering of the surface of previously tilted slabs
350 (B).
351
352 IBE2 happened on 09.08.2018. Figure 8b depicts the changes that occurred between 4:35 pm
353 and 4:58 pm. At this event three different processes were identified: (A) detachment of a
354 debris-covered ice peninsula (945 m²) from Pasterze Glacier at the western lakeshore and
355 separation into four icebergs (total area 1054 m²), (B) emergence of a 1035 m² large iceberg
356 (4:35-4:40 pm) followed by capsizing and partially disintegration of this iceberg into ice debris
357 (4:40-4:58 pm) pushing away other icebergs which cause (C) lateral iceberg displacement of up
358 to 65.6 m as well as a clockwise iceberg rotation of 95°.
359
360 IBE3 occurred on 26.09.2018. This event involved four main processes as visualised in Fig. 8c:
361 (A) uplift of debris-covered ice bodies increasing the surface area from 6820 to 13245 m² in
362 only 10 minutes (at 2:35-2:45 pm), (B) emergence of a new iceberg between 2:35 and 2:40
363 which capsized a few minutes afterwards, (C) limnic transgression, and (D) lateral iceberg
364 displacement (both at 2:35-3:00 pm). At the southern part of the affected area, icebergs moved
365 away from the uplifting area (push effect). In contrast, at the eastern part of the affected area
366 icebergs moved towards the uplifting area possibly due to compensatory currents causing a
367 suction effect. A large iceberg (IB1 in Fig. 7c) was hardly moving at all suggesting grounding
368 conditions.
369



370 The last major IBE took place on 24.10.2018 (IBE4) spanning only 5 minutes (Fig. 8d). Like IBE2,
371 a debris-covered ice peninsula (1,933 m²) detached from Pasterze Glacier at the western
372 lakeshore and separated into several icebergs (A). Furthermore, (B) ice disintegration and (C)
373 lateral iceberg displacement was observed during the event. The large iceberg IB1 experienced
374 a lateral offset of 22 m accompanied by a clockwise rotation by 43°. Spatial extent, volume and
375 freeboard of this iceberg was calculated based on a high-resolution DTM derived from the
376 aerial survey dating to 15.11.2018 (cf. Table 1). The subaerial volume of iceberg IB1 was 3271
377 m³ on 15.11.2018, which should be around 10% of the entire iceberg. Hence, some 29,500 m³
378 (90%) were during that time below the lake level. Maximum freeboard of IB1 was 3.7 m with a
379 mean freeboard value of 1.4 m. If we assume the same surface area of the iceberg below lake
380 level (2287 m²), we could further assume a mean ice thickness of the iceberg of 14.3 m (12.9 m
381 draft, 1.4 m freeboard). Therefore, in order to have a freely moveable iceberg, a water depth
382 exceeding 13 m is needed.

383

384 No large buoyant calving events were detectable in the time-lapse images after 24.10.2018.
385 However, at least the occurrence of small-sized buoyant calving events which are hardly
386 detectable by the time-lapse camera can be assumed. During field work in June 2019, we
387 observed buoyant calving of a small, c.3 m long iceberg (“shooter” according to Benn and
388 Evans, 2010) c.200 m from the subaerial glacier front (Fig. 3d). The whole event took only few
389 minutes and was hardly visible in the time-lapse images of that particular day.

390

391 **4.4. Ground ice conditions at the lake basin and its proximity**



392 Altogether 43 ERT profiles were measured in the proglacial area between 2015 and 2019 with
393 profile lengths of between 80 and 196 m. In this study we focus on the quantification of
394 sediment-buried dead ice bodies detected by ERT. A detailed discussion on the ERT results will
395 be presented elsewhere. Resistivity values $>20,000$ Ohm m indicate buried glacier ice and
396 water-saturated glacial sediments show values $<3,000$ Ohm m (Pant and Reynolds, 2000). Clay
397 and sand have resistivity values in the ranges of 1-100 and 100-5,000 Ohm m, respectively.
398 Temperate glacier ice may exceed 1×10^6 Ohm m (Kneisel and Hauck, 2008). We used the
399 20,000 Ohm m-boundary in the interpretation to estimate the maximum ice thickness for each
400 profile as depicted in Fig. 9 which shows three profiles from 2017. In many cases, ice thickness
401 exceeded the depth of ERT penetration. Therefore, we only were able to calculate “minimum
402 ice thickness estimates” based on the ERT data.

403

404 Figure 10 summarises the results of the surveys for 2015, 2016, 2017, 2018 and September
405 2019. Two of the three ERT profiles measured in 2015 (ERT15-1, ERT15-2) revealed only very
406 thin ice lenses. Both are located outside the proglacial basin as defined in September 2019 (Fig.
407 10a). The profile in the basin had an estimated ice thickness of 14 m (ERT15-3). The profiles
408 measured in 2016 revealed minimum ice thickness values of 8-10 m (Fig. 10b). The four profiles
409 measured in 2017 in the central part of the proglacial area revealed minimum ice thicknesses of
410 between 13 (ERT17-4) and 28 m (ERT17-2) (Fig. 10c) confirming the existence of massive dead
411 ice beneath a thin veneer of debris (Fig. 9).

412



413 The interpretation of four profiles measured in 2018 are shown in Fig. 10d. Profiles ERT18-2 and
414 ERT18-3 are free of ice located outside the basin or at its margin. ERT18-4 and ERT18-5 were
415 both located in the basin and revealed minimum ice thicknesses of 13 (ERT18-5) and 14 m
416 (ERT18-4). The September-2019 measurements supported earlier measurements (Fig. 10e). The
417 profiles at the eastern margin of the basin showed again a thin layer (ERT19-18; 8m ice) or only
418 very small occurrences of glacier ice (ERT19-19; 1 m ice). The three profiles near the north-
419 western shore of the lake revealed minimum ice thickness estimates of up to 26 m (ERT19-26).
420 In summary, ERT profiles outside the proglacial basin typically showed little buried dead ice
421 remnants, whereas profiles in the basin (particularly at its north-western part) typically yielded
422 resistivity values consistent with widespread massive dead ice.

423

424 **4.5. Bathymetry of the lake basin**

425 Lake bottom geometry and water volume of Lake Pasterzensee was calculated based on 4276
426 sonar measurements (Fig. 1d). Measured water depths ranged from 0.35 m to 48.2 m yielding
427 an arithmetic mean of 13.4 m and a median of 10.7 m. During the time of bathymetric
428 measurements, the lake level was 2069.1 m asl implying that the lowest point at the lake
429 bottom was 2020.9 m asl (Fig. 11a). Several sub-basins (marked as A-D in Fig. 11a) were
430 identified along the 1.2 km long and up to 300 m wide lake basin. One small sub-basin (A) was
431 detected close to the southern end of the lake with maximum measured water depths
432 exceeding 20 m (maximum 24.1 m, 2045 m asl), an E-W extent of 160 m, and a N-S dimension
433 of 140 m. A second sub-basin (B) is slightly less deep (max. 20.5 m) but seems to be broader
434 compared to basin (A). The third sub-basin (C) is by far the deepest, the largest, and the most



435 complex one with a maximum water depth of 48.2 m and a secondary basin in the south
436 reaching a measured maximum depth of 31.0 m. In this sub-basin, water depths exceeding 30
437 m were calculated for a 34,000 m² large in the central part of the entire lake basin. The lake
438 basin gets generally shallower towards the northwest. Finally, a fourth sub-basin (D) was
439 identified at the north-western end of Lake Pasterzensee where a broad basin is located with a
440 maximum measured depth of 17.7 m. Based on our gridded DTM for the lake bottom, the
441 estimated water volume of the 299,496 m² large Lake Pasterzensee in September 2019 was 4 x
442 10⁶ m³. The gradient from the deep basin (C) to the shore seems to be rather gradual at the
443 eastern margin of the lake. In contrast, at the western margin of the lake basin where Lake
444 Pasterzensee is in ice-contact, the gradient is steep in most areas (e.g. at sub-basin C: horizontal
445 distance between sonar measurement location and glacier margin 19 m vs. water depth 26.1m)
446 suggesting a steep glacier margin with a pronounced ice foot.

447

448 **5. DISCUSSION**

449 **5.1. Glacial-to-proglacial landscape modification**

450 Pasterze Glacier receded by some 1.4 km between 1998 and 2019 thereby causing the
451 formation of a bedrock-dammed lake in an over-deepened glacial basin. During these two
452 decades, the glacier decelerated, fractured (Kellerer-Pirklbauer and Kulmer, 2019) and lost the
453 connection to the lake at its eastern part. In contrast, at the western shore, the lake was still in
454 ice contact with the glacier in 2019. This ice-contact difference is related to an unequal
455 recession pattern of the eastern and western part of the glacier tongue caused by an uneven
456 distribution of the supraglacial debris cover (Kellerer-Pirklbauer, 2008). The debris cover



457 distribution pattern promotes differential ablation (Kellerer-Pirklbauer et al., 2008). Rapid
458 deglaciation as well as glacier thinning is much more intensive at the debris-poor part of the
459 glacier affecting the stress and strain field and modifying the flow directions of the ice mass
460 (Kaufmann et al., 2015). Therefore, the proglacial lake predominantly developed in areas where
461 debris-poor ice was located before.

462

463 At the waterline, thermo-erosional undercutting causes the formation of notches (cf. Röhl,
464 2006). Such notches are frequent features at Pasterze Glacier, and were first reported in 2004
465 (Kellerer-Pirklbauer, 2008). DGPS measurements at the glacier margin on 13.09.2019 showed
466 that waterline notches occurred during that time at 53% of the 935 m long ice-contact line
467 between Pasterze Glacier and Lake Pasterzensee (Fig. 5n). Notches observed at Pasterze Glacier
468 during several September-field-campaigns during the last years had a stepped geometry due to
469 lake-level drop. The amplitude of water-level fluctuations at Pasterzensee is in the order of one
470 meter during the summer months as shown by lake level measurements (pers. comm. Jakob
471 Abermann; cf. methods section). Stepped geometries were observed also at other alpine lakes
472 (e.g. Röhl 2006). Rates of notch formation and, thus, thermo-erosional undercutting at Pasterze
473 Glacier are unknown. However, if we consider the annual lateral backwasting rates derived
474 from DGPS (Fig. 4) as indicative for thermo-erosional undercutting, a mean melt rate of about
475 10 m yr^{-1} for the period 2010-2019 can be assumed. This is about one third of the values
476 quantified for Tasman Glacier (Röhl, 2006). The difference is possibly related to cooler (higher
477 elevation) and more shaded (NE-facing) conditions at Pasterze Glacier. Outward toppling of
478 undercut ice masses due to thermal erosion, a process potentially relevant for calving at ice-



479 contact lakes (Benn and Evans 2010), was not observed at Pasterze Glacier. Lateral backwasting
480 at Pasterze Glacier is mainly controlled by ice melting either beneath supraglacial debris or at
481 bare ice cliffs above notches where the slope is too steep to sustain a debris cover and thus the
482 rock material slides into the lake (see Fig. 10 in Kellerer-Pirklbauer, 2008).

483

484 The analysis of the relationship between glacier recession and the evolution of proglacial water
485 surfaces showed drastic changes in 1998-2019. The spatial extent of water surfaces in the 0.37
486 km² proglacial basin followed an exponential curve with 0.5% water surfaces in 1998, 21% by
487 2013, 51% by 2016, and 83% by 2019. On an annual timescale water surface changes follow a
488 distinct pattern with enlargement during summer due to glacier and dead-ice ablation in lake-
489 contact locations causing lake transgression and a shrinkage in size in autumn due to lake level
490 lowering. This annual pattern at Lake Pasterzensee has been also detected and quantified by
491 Sentinel-1 and Sentinel-2 data (Avian et al., 2020).

492

493 Carrivick and Tweed (2013) discuss the enhanced ablation at ice-contact lakes via mechanical
494 and thermal stresses at the glacier-water interfaces. They report increasing lake sizes in the
495 proglacial area of Tasersuaq Glacier, west Greenland, for four different stages between 1992
496 and 2010. An exponential increase in lake size, as observed at Pasterze Glacier, was however
497 not observed at Tasersuaq Glacier as judged from their provided map in the paper. More
498 general, detailed studies of increasing lake size on an annual basis are rare impeding the
499 comparison of our results with other studies accomplished in similar topoclimatical settings.
500 Some comparative observations are, however, as follows.



501

502 Schomacker and Kjær (2008) report from a glacier in Svalbard that an ice-contact lake increased
503 near-exponentially in size during a period of 40 years due to dead-ice melting. Schomacker
504 (2010) report from the enlargement of proglacial lakes at Vatnajökull in Iceland where the lake
505 Jökulsárlón enlarged by 40% in only 9 years (2000-2009). For the same lake, Canas et al. (2015)
506 revealed an enlargement by 74% for the period 1999-2014. Stockes et al. (2007) report an 57%
507 increase in the surface area of supra- and proglacial lakes in the Caucasus Mountains in the
508 period 1985-2000. Loriaux and Casassa (2012) described the evolution of glacial lakes from the
509 Northern Patagonia Icefield reporting a total lake area increase of 64.9% in a 66-year period
510 (1945-2011). Gardelle et al. (2011) detected for the Eastern Himalaya an enlargement of glacial
511 lakes by 20% to 65% between 1990 and 2009. To conclude, the numbers summarised here
512 clearly show that the increase in lake size at Pasterze Glacier is particularly high although this
513 relative increase in area at Lake Pasterzensee is likely biased by the very small initial size of the
514 lake in 1998.

515

516 Landscape changes were quantified for a 0.76 km² large transition zone between Pasterze
517 Glacier and its foreland for the period 1998-2019. Apart from rapid deglaciation and lake size
518 increase, areas covered by coarse-grained glacio-fluvial sediments increased in their extent.
519 Furthermore, icebergs in the lake were mapped for the first time in 2015 (0.7% of the 0.76 km²
520 large area) and reached their maximum extent in 2018 (3.5%). By the end of the ablation
521 season in 2019, the areal extent of icebergs decreased dramatically to only 0.3% attributed to
522 high melt rates in a warm summer 2019 (Fig. 1c: the MAAT in 2019 was the second highest in



523 the period 1998-2019). After 2015, an alluvial fan with a lake delta developed at the northern
524 end of the lake because the glacier receded at this location from the lake basin connecting the
525 main glacial stream directly with the lake (Fig. 6f and g). This recession was, however, only
526 superficial, and huge amounts of dead ice remained in the basin – as detected by ERT
527 measurements – and were covered by fluvio-glacial sediments.

528

529 **5.2. Dead-ice conditions and changes**

530 Subsurface conditions at the proglacial area of Pasterze Glacier were studied by measuring
531 electrical resistivity along 43 profiles distributed over the entire proglacial area between 2015
532 and 2019. Our measurements showed that dead ice bodies covered by sediments were absent
533 outside the proglacial basin as defined for September 2019. In contrast, all ERT measurements
534 carried out in the basin revealed very high maximum and median resistivity values (e.g. Fig. 9)
535 indicative of buried ice. Long-term air temperature data from a nearby automatic weather
536 station as well as two ground temperature data series directly from the proglacial area clearly
537 suggest that permafrost is absent at the shores of Lake Pasterzensee due to permafrost-
538 unfavourable thermal conditions (MAAT always $>2.5^{\circ}\text{C}$ since 2011). Furthermore, a distinct
539 warming trend occurred in the period 1998-2019 at Pasterze Glacier enhancing ice ablation and
540 deglaciation processes at the surface and the surface in more recent years.

541

542 In addition to the geomorphic observations made at the surface such as dead-ice holes (Figs 6b
543 and 7) or cracks (Fig. 2) in hummocky fluvio-glacial sediments (Fig. 3c), our subsurface data
544 clearly suggest substantial and rapid dead-ice degradation at present. Gärtner-Roer and Bast



545 (2019) conclude that only a few attempts have been made to describe and analyse the
546 occurrence, distribution, and dynamics of ground ice in recently deglaciated areas. However,
547 due to the rapid increase in proglacial areas at present, these authors point out that there is
548 increasing interest on research both for geomorphologist and hydrologists. With the presented
549 geophysical data from Pasterze Glacier, we proved the widespread existence of debris-covered
550 dead-ice bodies in a proglacial basin of an alpine valley glacier and, thus, contribute to this
551 emerging topic.

552

553 **5.3. Ice-breakup and buoyant calving**

554 Four remarkable ice-breakup events (IBE) with horizontal extents in the order of hundreds of
555 meters occurred in the period September 2016 to October 2018. No comparable events were
556 observed before the 20.09.2016 (Kellerer-Pirklbauer et al., 2017) and no comparable event
557 happened between 25.10.2018 and 29.07.2020. Only smaller buoyant calving events can be
558 assumed for the latter period as suggested by a fortuitously observed event (Fig. 3d).

559

560 Thanks to high-resolution (both spatial and temporal) time lapse photography overlooking the
561 glacial-proglacial transition zone, different ice-related processes can be clearly distinguished.

562 Common features of the IBEs are (a) limnic transgression due to ice slab lowering or tilting, (b)
563 drying out of meltwater channels due to slab uplift or tilting of ice slabs, (c) uplift – and
564 therefore enlargement – of previously existing ice-cored terraces or icebergs, (d) crack and
565 crevasse formation at previously stable-looking terraces, (e) sudden disintegration of ice
566 masses (i.e. collapsing ice masses) within minutes into ice debris, (f) lateral displacement of



567 icebergs (either pushed away or dragged towards uplifting icebergs), (g) emerging new icebergs
568 previously not mapped due to buoyant calving, (h) capsizing of new icebergs, and (i)
569 detachment of “ice peninsulas” attached to Pasterze Glacier at the western lakeshore and
570 subsequent fragmentation into several icebergs and disintegration into small, mainly floating
571 icebergs. Regarding emergence of new icebergs, our observations suggest both buoyant calving
572 of small ice masses (suggested by emerging small icebergs, e.g. Fig. 3d) but also full-thickness
573 ice calving (suggested by the large ice-breakup events; Fig. 8).

574

575 All these processes are related to hydrostatic disequilibrium of the glacier margin or subaquatic
576 dead ice which becomes super-buoyant and subject to net upward buoyant forces (Benn et al.,
577 2007). Buoyant glacier margins can slowly move back into equilibrium by ice creep or can
578 fracture catastrophically as described for instance for Glacier Nef in Chile by Warren et al.
579 (2001). At Pasterze, creep rates are very low at the glacier margin with only few meters per
580 year near the terminus (Kellerer-Pirklbauer and Kulmer, 2019) therefore only the latter option
581 for a renewed hydrostatic equilibrium is feasible. A floating process of the glacier terminus was,
582 however, not observed at Pasterze Glacier (Boyce et al., 2007). Our buoyant calving
583 observations as well as the bathymetric data suggest the existence of an ice foot at the west
584 shore of the ice-contact lake. Such a presence of an ice foot below the water level of tidewater
585 ice cliffs of temperate glaciers has been debated for more than 120 years (Hunter and Powell,
586 1998). At Pasterze Glacier only small ice cliffs above thermo-erosional notches exist. However,
587 the existence of an ice foot at the western shore is very likely. This assumption is supported by
588 the occurrence of the ice breaking events with buoyant calving-related processes.



589

590 In summary, we identified the following sequence of processes at Pasterze Glacier: (a) glacier
591 recession into an overdeepened basin and glacier thinning below spillway-level; (b) glacio-
592 fluvial sedimentation in the glacial-proglacial transition zone covering dead ice; (c) initial
593 formation and accelerating enlargement of a glacier-lateral to supraglacial lake by ablation of
594 glacier ice and debris-covered dead ice forming thermokarst features; (d) increase in
595 hydrostatic disequilibrium leading to general glacier-ice instability; (e) destabilization of debris-
596 buried ice at the lake shore expressed by fracturing, tilting, and disintegration due to buoyancy;
597 (f) emergence of new icebergs due to buoyant calving; (g) gradual melting of icebergs along
598 with iceberg capsizing events. This sequence of processes is visualized in a conceptual model
599 depicted in Fig. 12. Our observations suggest that buoyant calving, previously not reported
600 from the European Alps, might play an important role at alpine glaciers in the future as many
601 glaciers are expected to recede into valley overdeepenings or cirques.

602

603 **6. CONCLUSIONS**

604 We studied the glacial-to-proglacial landscape transformation at the largest glacier in Austria
605 during the period 1998 to 2019 focusing on ice-contact lake evolution and buoyant calving
606 processes in an overdeepened basin. The main conclusions which can be drawn from this study
607 are the following:

- 608 • High annual backwasting rates were measured in most years when the glacier
609 terminated in the basin. The detachment of the glacier from the lake at the east side
610 drastically reduced backwasting rates.



- 611 • Detailed studies of increasing lake size on an annual basis are rare. We showed that the
612 increase in water surfaces in the basin since 1998 follows an exponential curve (1998:
613 1900 m²; 2019: 0.3 km²). The increase in lake size is particularly high although this
614 pattern is likely biased by the very small initial size of the lake in 1998. In single years
615 this areal increase follows a distinct pattern with enlargement of water surfaces during
616 summer and a decrease in autumn due to lake-level lowering supporting earlier
617 satellite-based studies (Avian et al. 2020).
- 618 • Icebergs in the up to 48.2 m deep lake were observed for the first time in 2015 and
619 reached their maximum extent in 2018. By the end of the ablation season in 2019, the
620 areal extent of icebergs decreased dramatically, attributed to high melt rates in a warm
621 summer 2019.
- 622 • Both, geomorphic observations made at the surface and geophysical data from the
623 subsurface clearly suggest widespread existence of debris-covered dead-ice bodies in
624 the proglacial basin which is substantially and rapidly affected by dead-ice degradation
625 at present due to permafrost-unfavourable ground temperature conditions.
- 626 • Previously, little was known about how buoyant calving might contribute to the
627 transformation of supraglacial lakes into full-depth lakes lacking any ice at the lake
628 bottom. Thanks to time-lapse images and photogrammetric data analysis, we were able
629 to analyse four large-scale ice-breakup events related to ice buoyancy for the period
630 September 2016 to October 2018. However, no large buoyant calving events were
631 detectable in the time-lapse images after 24.10.2018 and until (at least) 29.07.2020.



632 • Different ice-related processes related to hydrostatic disequilibrium have been
633 identified: limnic transgression due to ice slab lowering or tilting; drying out of
634 meltwater channels due to slab uplift or tilting of ice slabs; uplift and enlargement of
635 ice-cored terraces or icebergs; crack formation at previously stable-looking terraces;
636 sudden disintegration of ice masses into ice debris; lateral displacement or rotation of
637 icebergs; emergence of new icebergs due to buoyant calving; capsizing of icebergs;
638 detachment of ice peninsulas attached to the glacier and subsequent fragmentation into
639 several icebergs.

640 • Our observations suggest that buoyant calving, previously not reported from the
641 European Alps, might play an important role at alpine glaciers in the future as many
642 valley and cirque glaciers are expected to recede into valley overdeepenings or corries.

643

644 **Data availability.** The data sets used in this study will be available in a data repository not
645 specified yet.

646

647 **Author contributions.** The study was designed by AKP. Fieldwork and analysis were carried out
648 by AKP (GNSS, geophysics, bathymetry), MA (laserscanning), FB (time-lapse photography), PK
649 (land cover mapping), CZ (geophysics, bathymetry). DIB contributed to the introduction and
650 discussion. AKP prepared the manuscript with contributions from all co-authors

651

652 **Competing interests.** The authors declare that they have no conflict of interest.

653



654 **Acknowledgments.** This study was funded by different projects over the years. The most
655 important ones are: (a) Austrian Science Fund, project no. FWF P18304-N10, (b) Hohe Tauern
656 National Park authority (several projects), (c) Glockner Ökofonds (GROHAG) 2018, and (d)
657 Austrian Alpine Association (through the annual glacier monitoring program). Meteorological
658 data were kindly provided by Austrian Hydro Powers. Aerial surveys of 2018 and 2019
659 (AeroMap) were funded by project (c) and the Institute of Geography and Regional Science
660 (supported by Wolfgang Sulzer). Matthias Wecht, Gernot Seier and Wolfgang Sulzer are very
661 much thanked for supporting the aerial photograph analysis of the two AeroMap flight
662 campaigns in 2018 and 2019. Correction signals for RTK measurements were kindly provided
663 free of charge by EPOSA, Vienna. Field work was supported during numerous field trips by
664 several colleagues and numerous students especially Michael Bliem, Stefan Brauchart,
665 Alexander Dorić, Iris Hansche, Matthias Lichtenegger, Christian Lieb, Gerhard Karl Lieb,
666 Matthias Rathofer, Rupert Schwarzl, and Daniel Winkler. Finally, the authors acknowledge the
667 financial support by the University of Graz.

668

669 **ORCID**

670 Andreas Kellerer-Pirklbauer <https://orcid.org/0000-0002-2745-3953>

671

672



673 **REFERENCES**

- 674 Avian, M., Lieb, G. K., Kellerer-Pirklbauer, A., and Bauer, A.: Variations of Pasterze Glacier (Austria)
675 between 1994 and 2006 - combination of different data sets for spatial analysis, in: Proceedings of the
676 9th International Symposium of High Mountain Remote Sensing Cartography, Graz, Austria, 14-22
677 September 2006, 79-88, 2007.
- 678 Avian, M., Kellerer-Pirklbauer, A., and Lieb, G. K.: Geomorphic consequences of rapid deglaciation at
679 Pasterze Glacier, Hohe Tauern Range, Austria, between 2010 and 2013 based on repeated terrestrial
680 laser scanning data, *Geomorphology*, 310, 1-14, <https://doi.org/10.1016/j.geomorph.2018.02.003>, 2018.
- 681 Avian, M., Bauer, C., Schlögl, M., Widhalm, B., Gutjahr, K.H., Paster, M., Hauer, C., Frießenbichler, M.,
682 Neureiter, A., Weyss, G., Flödl, P., Seier, G., and Sulzer, W.: The status of earth observation techniques in
683 monitoring high mountain environments at the example of Pasterze Glacier, Austria: data, methods,
684 accuracies, processes, and scales, *Remote Sens-Basel*, 12, 1251, <https://doi.org/10.3390/rs12081251>,
685 2020.
- 686 Ballantyne, C. K.: Paraglacial geomorphology, *Quaternary Science Reviews*, 21, 1935-2017,
687 [https://doi.org/10.1016/S0277-3791\(02\)00005-7](https://doi.org/10.1016/S0277-3791(02)00005-7), 2002.
- 688 Benn, D. I., Wiseman, S., and Hands, K. A.: Growth and drainage of supraglacial lakes on the debris-
689 mantled Ngozumpa Glacier, Khumbu Himal, Nepal, *J Glaciol*, 47, 626-638,
690 <https://doi.org/10.3189/172756501781831729>, 2001.
- 691 Benn, D. I. and Evans D. J. A.: *Glaciers and Glaciation*, 2nd edn. Hodder/Arnold Publication, London, UK,
692 2010.
- 693 Bernsteiner, F.: *Dynamik von Eisbruchprozessen im proglazialen See der Pasterze*. Bachelor Thesis,
694 University of Graz, Graz, 54 pp., 2019.
- 695 Bosson, J.B., Deline, P., Bodin, X., Schoeneich, P., Baron, L., Gardent, M., and Lambiel, C.: The influence
696 of ground ice distribution on geomorphic dynamics since the Little Ice Age in proglacial areas of two
697 cirque glacier systems. *Earth Surf Process Land*, 40, 666-680, <https://doi.org/10.1002/esp.3666>, 2015.
- 698 Boyce, E.S., Motyka, R.J., and Truffer, M.: Flotation and retreat of a lake-calving terminus, Mendenhall
699 Glacier, southeast Alaska, USA. *J Glaciol*, 53, 211-224, <https://doi.org/10.3189/172756507782202928>,
700 2007.
- 701 Buckel, J., Otto, J. C., Prasicek, G., and Keuschnig, M.: Glacial lakes in Austria - distribution and formation
702 since the Little Ice Age, *Global Planet Change*, 164, 39-51,
703 <https://doi.org/10.1016/j.gloplacha.2018.03.003>, 2018.
- 704 Buckel, J. and Otto J. C.: The Austrian Glacier Inventory GI 4 (2015) in ArcGis (shapefile) format.
705 PANGAEA, <https://doi.org/10.1594/PANGAEA.887415>, 2018.



- 706 Canas, D., Chan, W. M., Chiu A., Jung-Ritchie L., Leung M., Pillay L., and Waltham B.: Potential
707 environmental effects of expanding Lake Jökulsárlón in response to melting of Breiðamerkurjökull,
708 Iceland, *Cartographica*, 50, 204-213, <https://doi.org/10.3138/cart.50.3.3197G>, 2015.
- 709 Carrivick, J. L. and Tweed F. S.: Proglacial lakes: character, behaviour and geological importance, *Quatern*
710 *Sci Rev*, 78, 34-52, <https://doi.org/10.1016/j.quascirev.2013.07.028>, 2013.
- 711 Carrivick J. L. and Heckmann T.: Short-term geomorphological evolution of proglacial systems,
712 *Geomorphology*, 287, 3-28, <https://doi.org/10.1016/j.geomorph.2017.01.037>, 2017.
- 713 Dykes, R. C., Brook, M. S., and Winkler, S.: The contemporary retreat of Tasman Glacier, Southern Alps,
714 New Zealand, and the evolution of Tasman proglacial lake since AD 2000, *Erdkunde*, 141-154,
715 <https://doi.org/10.3112/erdkunde.2010.02.03>, 2010.
- 716 Gardelle, J., Arnaud, Y., and Berthier, E.: Contrasted evolution of glacial lakes along the Hindu Kush
717 Himalaya mountain range between 1990 and 2009. *Global Planet Change*, 75, 47-55,
718 <https://doi.org/10.1016/j.gloplacha.2010.10.003>, 2011.
- 719 Gärtner-Roer, I. and Bast, A.: (Ground) Ice in the proglacial zone: landform and sediment dynamics in
720 recently deglaciated alpine landscapes, in: *Geomorphology of proglacial systems, Geography of the*
721 *Physical Environment*, edited by Heckmann, T. and Morche D., Springer, Berlin, Heidelberg, Germany,
722 85-98, https://doi.org/10.1007/978-3-319-94184-4_6, 2019.
- 723 Hirschmann, S.: Die glaziale und proglaziale Übergangszone im Bereich zweier Gletscher in den Hohen
724 Tauern, Master Thesis, University of Graz, Graz, 106 pp., 2017.
- 725 Holdsworth, G.: Ice calving into the proglacial Generator Lake, Baffin Island, NWT, Canada. *J Glaciol*, 12,
726 235-250, 1973.
- 727 Hunter L. E., and Powell R. D.: Ice foot development at temperate tidewater margins in Alaska. *Geophys*
728 *Res Let*, 25, 1923-1926, <https://doi.org/10.1029/98GL01403>, 1998.
- 729 Kaufmann, V., Kellerer-Pirklbauer, A., Lieb, G. K., Slupetzky, H., and Avian, M.: Glaciological studies at
730 Pasterze Glacier (Austria) based on aerial photographs 2003-2006-2009, in: *Monitoring and Modelling of*
731 *Global Changes: A Geomatics Perspective*, edited by: Yang, X. and Li, J., Springer, Berlin, Heidelberg,
732 Germany, 173-198, https://doi.org/10.1007/978-94-017-9813-6_9, 2015.
- 733 Kellerer-Pirklbauer, A.: The supraglacial debris system at the Pasterze Glacier, Austria: spatial
734 distribution, characteristics and transport of debris, *Z. Geomorph. N.F.* 52, Suppl., 1, 3-25,
735 <https://doi.org/10.1127/0372-8854/2008/0052S1-0003>, 2008.
- 736 Kellerer-Pirklbauer, A. and Kulmer, B.: The evolution of brittle and ductile structures at the surface of a
737 partly debris-covered, rapidly thinning and slowly moving glacier in 1998–2012 (Pasterze Glacier,
738 Austria), *Earth Surf Processes*, 44, 1034–1049. <https://doi.org/10.1002/esp.4552>, 2019.



- 739 Kellerer-Pirklbauer, A., Lieb, G. K., Avian, M., and Gspurning, J.: The response of partially debris-covered
740 valley glaciers to climate change: The Example of the Pasterze Glacier (Austria) in the period 1964 to
741 2006, *Geogr Ann A*, 90 A/4, 269-285, <https://doi.org/10.1111/j.1468-0459.2008.00345.x>, 2008.
- 742 Kellerer-Pirklbauer, A., Avian, M., Hirschmann, S., Lieb, G. K., Seier, G., Sulzer, W., and Wakonigg, H.:
743 Sudden disintegration of ice in the glacial-proglacial transition zone of the largest glacier in Austria, EGU
744 General Assembly, Vienna, Austria, 23–28 April 2017, EGU2017-12069, 2017.
- 745 King, O., Dehecq, A., Quincey, D., and Carrivick, J.: Contrasting geometric and dynamic evolution of lake
746 and land-terminating glaciers in the central Himalaya. *Global Planet Change*, 167, 46-60,
747 <https://doi.org/10.1016/j.gloplacha.2018.05.006>, 2018.
- 748 King, O., Bhattacharya, A., Bhambri, R., and Bolch, T.: Glacial lakes exacerbate Himalayan glacier mass
749 loss, *Sci Rep*, 9, 18145, <https://doi.org/10.1038/s41598-019-53733-x>, 2019.
- 750 Kirkbride, M. P. and Warren, C. R.: Tasman Glacier, New Zealand: 20th-century thinning and predicted
751 calving retreat, *Global Planet Change*, 22, 11-28, [https://doi.org/10.1016/S0921-8181\(99\)00021-1](https://doi.org/10.1016/S0921-8181(99)00021-1), 1999.
- 752 Kneisel, C. and Kääh, A.: Mountain permafrost dynamics within a recently exposed glacier forefield
753 inferred by a combined geomorphological, geophysical and photogrammetrical approach. *Earth Surf*
754 *Proc Land*, 32, 1797–1810, <https://doi.org/10.1002/esp.1488>, 2007.
- 755 Kneisel, C. and Hauck, C.: Electrical methods, in: *Applied Geophysics in Periglacial Environments*, edited
756 by: Hauck, C. and Kneisel, C., Cambridge University Press, Cambridge, UK, 3-27,
757 <https://doi.org/10.1017/CBO9780511535628>, 2008.
- 758 Krisch, P. and Kellerer-Pirklbauer, A.: Landschaftsdynamik im glazialen-proglazialen Übergangsbereich
759 der Pasterze im Zeitraum 1998-2015, *Carinthia II*, 209./129, 565-580, 2019.
- 760 Lieb, G. K., and Kellerer-Pirklbauer, A.: Die Pasterze, Österreichs größter Gletscher und seine lange
761 Messreihe in einer Ära massiven Gletscherschwundes, in: *Gletscher im Wandel - 125 Jahre*
762 *Gletschermessdienst des Alpenvereins*, , edited by: Fischer, A., Patzelt, G., AchRAINER, M., Groß, G., Lieb,
763 G. K., Kellerer-Pirklbauer, A., and Bandler, G., Springer, Heidelberg, Germany, 31-51,
764 <https://doi.org/10.1007/978-3-662-55540-8>, 2018.
- 765 Liu, Q., Mayer, C., Wang, X., Nie, Y., Wu, K., Wei, J., and Liu, S.: Interannual flow dynamics driven by
766 frontal retreat of a lake-terminating glacier in the Chinese Central Himalaya. *Earth Planet Sc Lett*, 546,
767 116450, <https://doi.org/10.1016/j.epsl.2020.116450>, 2020.
- 768 Loke, M.H.: *Electrical imaging surveys for environmental and engineering studies – a practical guide to 2-*
769 *D and 3-D surveys*, Penang, Malaysia, 2000.
- 770 Otto, J. C.: Proglacial Lakes in High Mountain Environments, in: *Geomorphology of proglacial systems,*
771 *Geography of the Physical Environment*, edited by Heckmann, T. and Morche D., Springer, Berlin,
772 Heidelberg, Germany, 231-247, https://doi.org/10.1007/978-3-319-94184-4_14, 2019.



- 773 Pant, S. R. and Reynolds J. M.: Application of electrical imaging techniques for the investigation of
774 natural dams: an example from the Thulagi Glacier Lake, Nepal. *J Nepal Geolog Soc*, 22, 211-218, 2000.
- 775 Richardson, S. D. and Reynolds, J. M.: An overview of glacial hazards in the Himalayas, *Quatern Int*,
776 65/66, 31-47, [https://doi.org/10.1016/S1040-6182\(99\)00035-X](https://doi.org/10.1016/S1040-6182(99)00035-X), 2000.
- 777 Röhl, K.: Thermo-erosional notch development at fresh-water-calving Tasman Glacier, New Zealand. *J*
778 *Glaciol*, 52, 203-213, <https://doi.org/10.3189/172756506781828773>, 2009.
- 779 Seier, G., Kellerer-Pirklbauer, A., Wecht, W., Hirschmann, S., Kaufmann, V., Lieb, G. K., and Sulzer, W.:
780 UAS-based change detection of the glacial and proglacial transition zone at Pasterze Glacier, Austria,
781 *Remote Sens-Basel*, 9, 549, 1-19, <https://doi.org/10.3390/rs9060549>, 2017.
- 782 Schomacker, A.: Expansion of ice-marginal lakes at the Vatnajökull ice cap, Iceland, from 1999 to 2009.
783 *Geomorphology*, 119, 232-236, <https://doi.org/10.1016/j.geomorph.2010.03.022>, 2010.
- 784 Schomacker, A. and Kjær, K. H.: Quantification of dead-ice melting in ice-cored moraines at the high-
785 Arctic glacier Holmströmbreen, Svalbard, *Boreas*, 37, 211-225, [https://doi.org/10.1111/j.1502-](https://doi.org/10.1111/j.1502-3885.2007.00014.x)
786 [3885.2007.00014.x](https://doi.org/10.1111/j.1502-3885.2007.00014.x), 2008.
- 787 Stokes, C.R., Popovnin, V., Aleynikov, A., Gurney, S.D., Shahgedanova, M.: Recent glacier retreat in the
788 Caucasus Mountains, Russia, and associated increase in supraglacial debris cover and supra-/proglacial
789 lake development. *A Glaciol*, 46, 195-203, <https://doi.org/10.3189/172756407782871468>, 2007.
- 790 Wakonigg, H., and Lieb, G.K.: Die Pasterze und ihre Erforschung im Rahmen der Gletschermessungen,
791 *Kärntner Nationalpark-Schriften*, 8, Großkirchheim, 99-115, 1996.
- 792 Warren, C., Benn, D. I., Winchester V., and Harrison, S.: Buoyancy-driven lacustrine calving, *Glaciar Nef*,
793 *Chilean Patagonia, J Glaciol*, 47, 135-146, <https://doi.org/10.3189/172756501781832403>, 2001.
- 794 Zuo Z. and Oerlemans J.: Numerical modelling of the historic front variation and the future behaviour of
795 the Pasterze Glacier, Austria. *Ann Glaciol*, 24, 234-241, <https://doi.org/10.3189/S0260305500012234>,
796 1997.
- 797



798 **Tables and table captions**

799

800 **Table 1:** Technical parameters of aerial surveys between 1998 and 2019 used in this study. For
801 2003, 2006, and 2009 see also Kaufmann et al. (2015). KAGIS = GIS Service of the Regional
802 Government of Carinthia; BEV = Federal Office of Metrology and Surveying.

Aerial survey	Acquisition date	Source	Geometric resolution of calculated orthophotos
1998	Aug. 1998	National Park Hohe Tauern	0.5 m
2003	13.08.2003	Kaufmann et al. (2015)	0.5 m
2006	22.09.2006	Kaufmann et al. (2015)	0.5 m
2009	24.08.2009	Kaufmann et al. (2015)	0.5 m
2012	18.08.2012	KAGIS / BEV	0.2 m
2015	11.07.2015	KAGIS / BEV	0.2 m
2018	11.09.2018	KAGIS / BEV	0.2 m
2018	15.11.2018	AeroMap GmbH	0.1 m
2019	21.09.2019	AeroMap GmbH	0.09 m

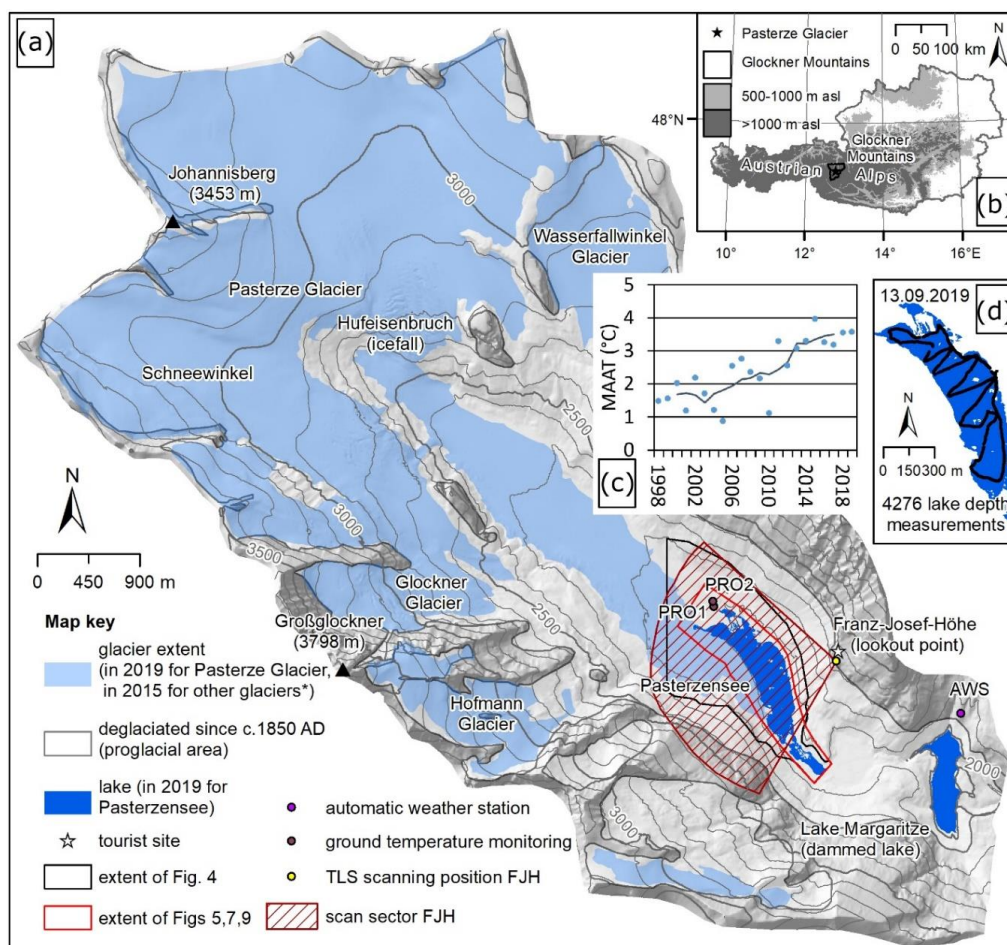
803

804

805

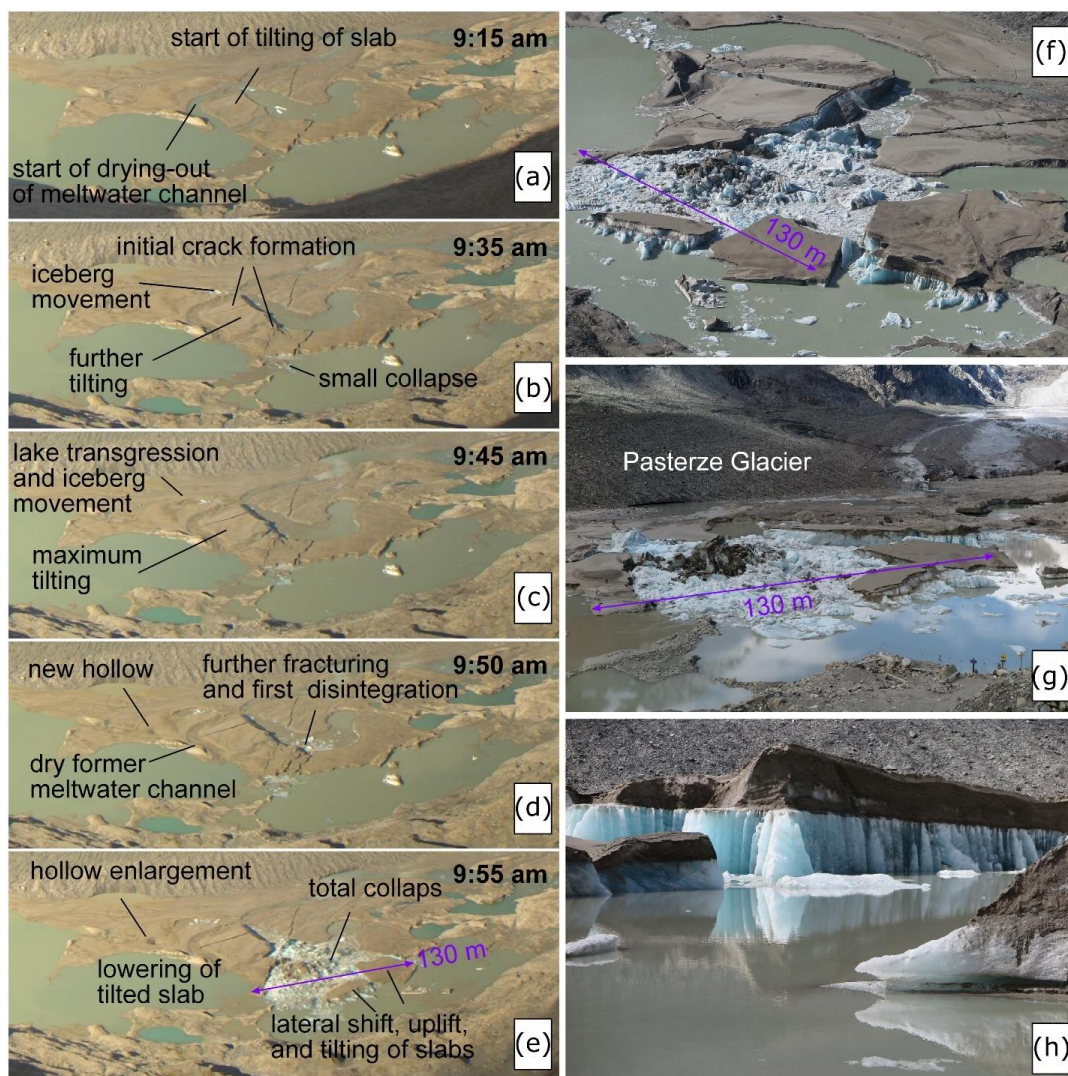


806 **Figures and figure captions**



807

808 **Figure 1:** Pasterze Glacier. (a) Location of Pasterze Glacier at the foot of Großglockner (3798m asl).
809 Relevant sites are indicated; (b) location of the study area within Austria; (c) mean annual air
810 temperature (MAAT) at the automatic weather station (AWS) Margaritze in 1998-2019 (single years and
811 5-year running mean); (d) position of 4276 lake depth measurements carried out on 13.09.2019.
812 Hillshade in the background of (a) from 2012 source KAGIS. Extent of glacier and lake in 2019 this study.
813 Glacier extent of 2015 (*) based on Buckel and Otto (2018). Glacier extent of c.1850 based on own
814 mapping.



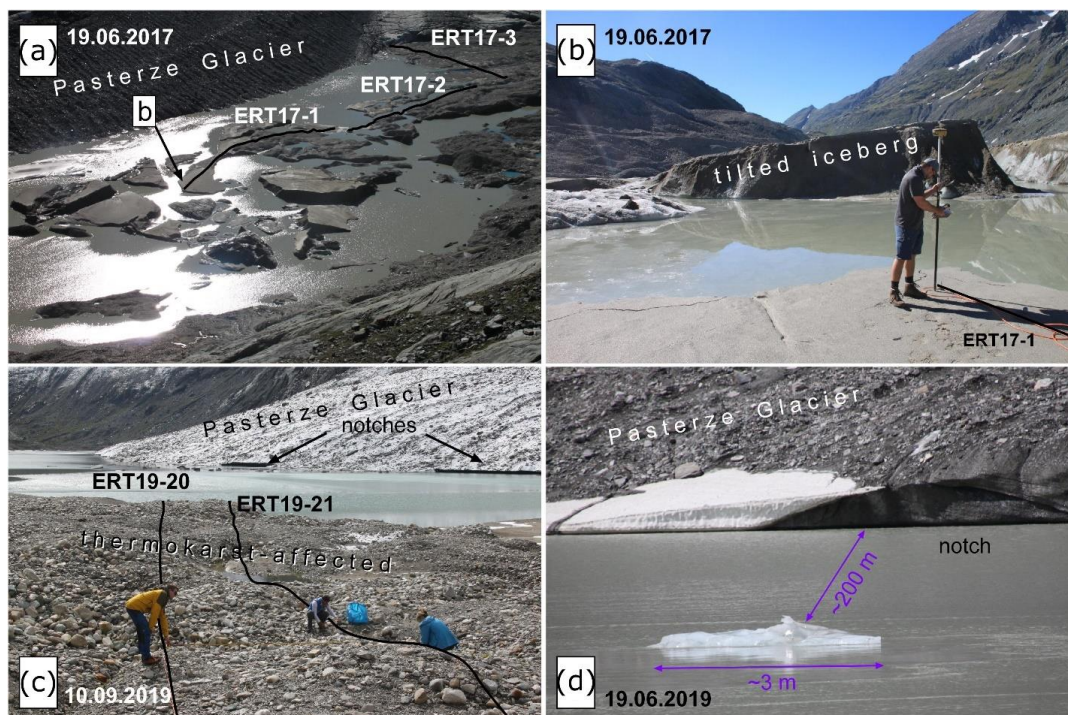
815

816 **Figure 2:** Evolution of the proglacial area at Pasterze Glacier during a period of only 40 minutes
817 (20.09.2016; from 9:15 to 9:55 a.m.) due to loss of hydrostatic disequilibrium and buoyancy as depicted
818 by an automatic time-lapse camera (a-e) and observed in the field a few hours after the event (f-h). Note
819 the sudden fracturing between 9:50 and 9:55 am. (a-e) provided by GROHAG, (f-h) provided by Konrad
820 Mariacher, 20.09.2016.

821



822



823

824 **Figure 3:** Field impressions of the ice-contact lake and its close surrounding: (a) overview image
825 depicting the distribution of water bodies, icebergs and debris-covered dead-ice bodies on 19.06.2017.
826 Courses of ERT profiles presented in Figure 9 are shown; (b) starting point of ERT17-1 surveyed by DGPS;
827 (c) thermokarst-affected area with courses of two ERT profiles on 10.09.2019. Note the Pasterze Glacier
828 and thermo-erosional notches at the lake level; (d) buoyant calving of a small iceberg (“shooter”) c.200
829 m from the subaerial glacier front observed during fieldwork (all photographs Andreas Kellerer-
830 Pirklbauer).

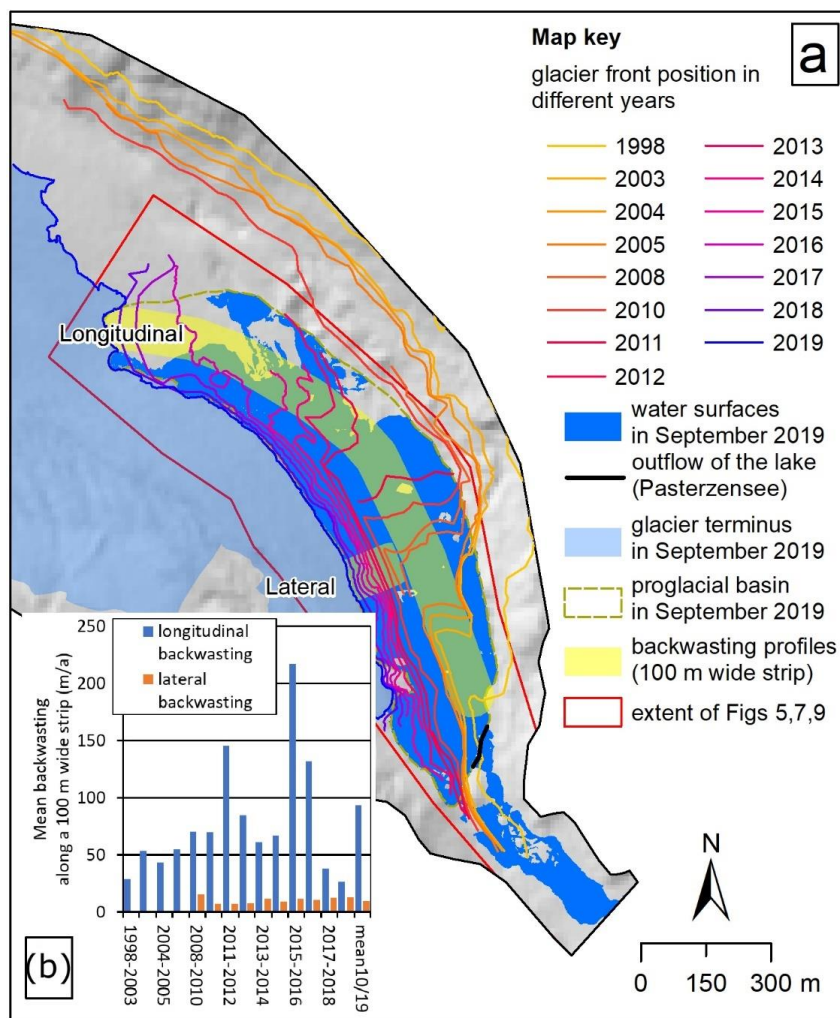
831

832

833

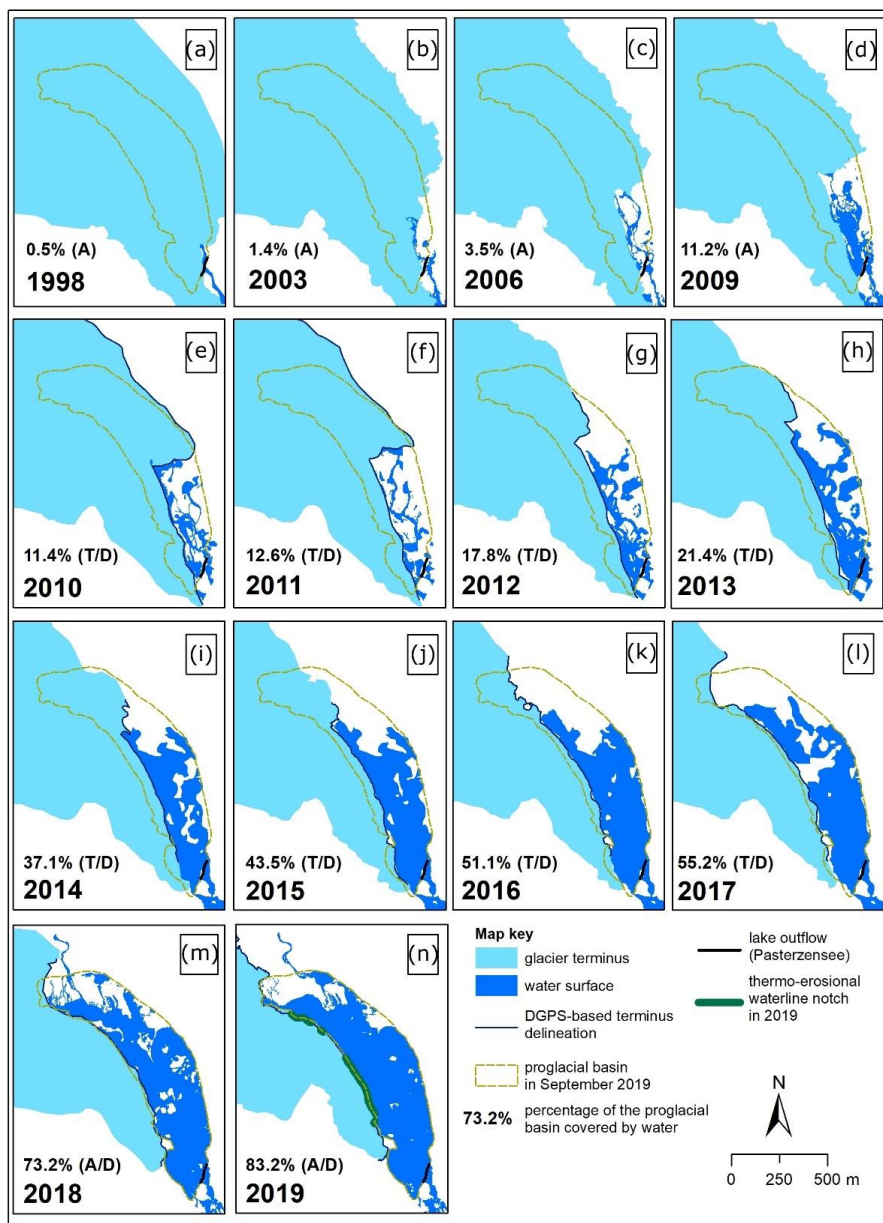


834



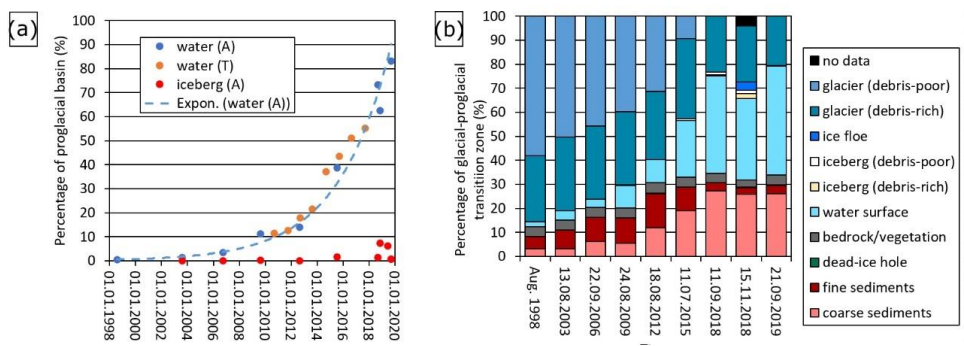
835

836 **Figure 4:** Terminus position of Pasterze Glacier for the period 1998 to 2019 derived mainly from
 837 sequential DGPS data. (a) the extent of water surfaces including the Lake Pasterzensee and the
 838 delineation of the proglacial basin is shown for September 2019. 100 m wide profiles (lateral and
 839 longitudinal) used for backwasting calculations are indicated. Backwasting results are depicted in (b)
 840 (background hillshade based on 10m DTM, KAGIS).



841

842 **Figure 5:** Glacier recession and evolution of proglacial water surfaces since 1998 at Pasterze Glacier. The
 843 proglacial basin as defined for September 2019 is depicted in all maps for comparison. For data sources
 844 refer to text and Table 1. A=airborne photogrammetry, T=terrestrial laserscanning, D=DGPS.



845

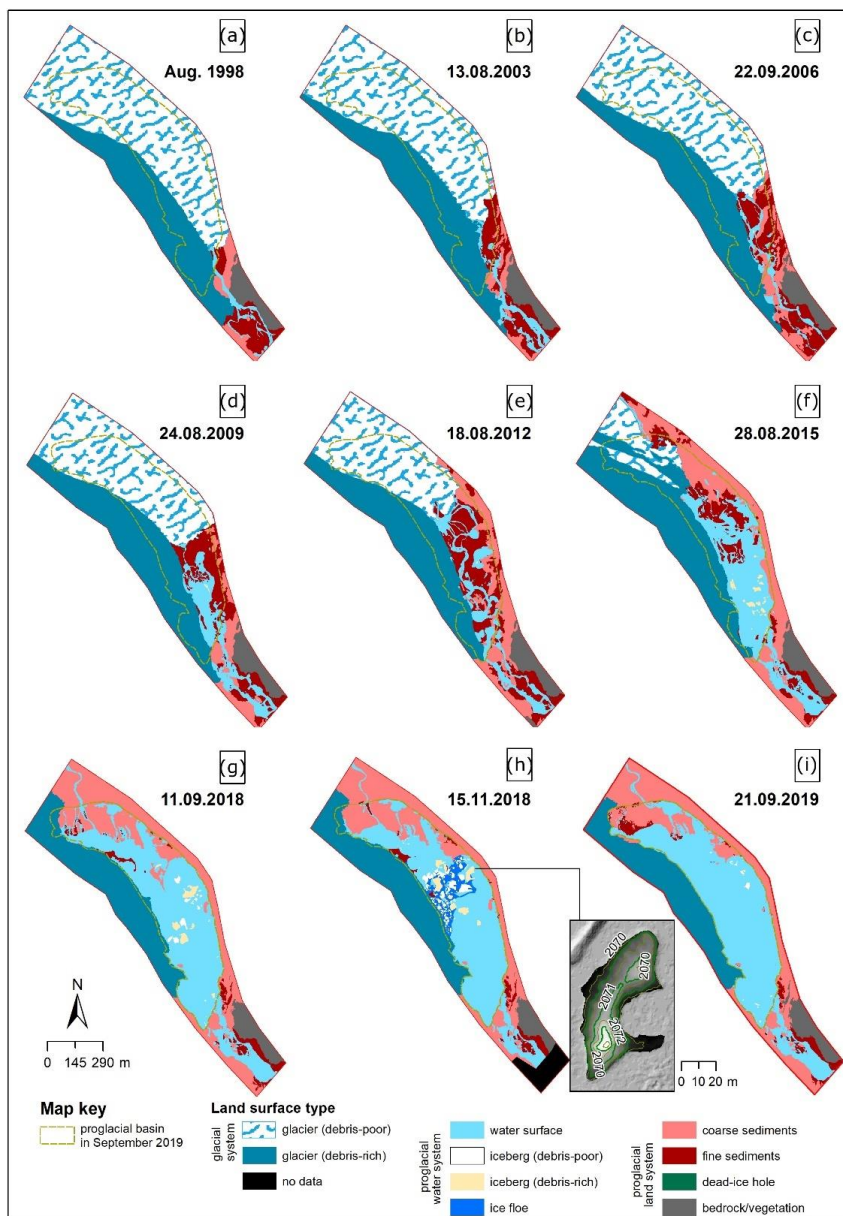
846 **Figure 6:** Glacial-proglacial transition zone: (a) Evolution of water surfaces and icebergs in the proglacial
 847 basin (100%=0.37 km²; Fig. 5 for delineation) of Pasterze Glacier since 1998 based on airborne
 848 photogrammetry/A or terrestrial laserscanning/T data. Icebergs only based on airborne
 849 photogrammetry/A; (b) summarising graph depicting relative changes of different surface types in the
 850 glacial-proglacial zone (100%=0.76 km²; extent as shown in Fig. 7) since 1998.

851

852

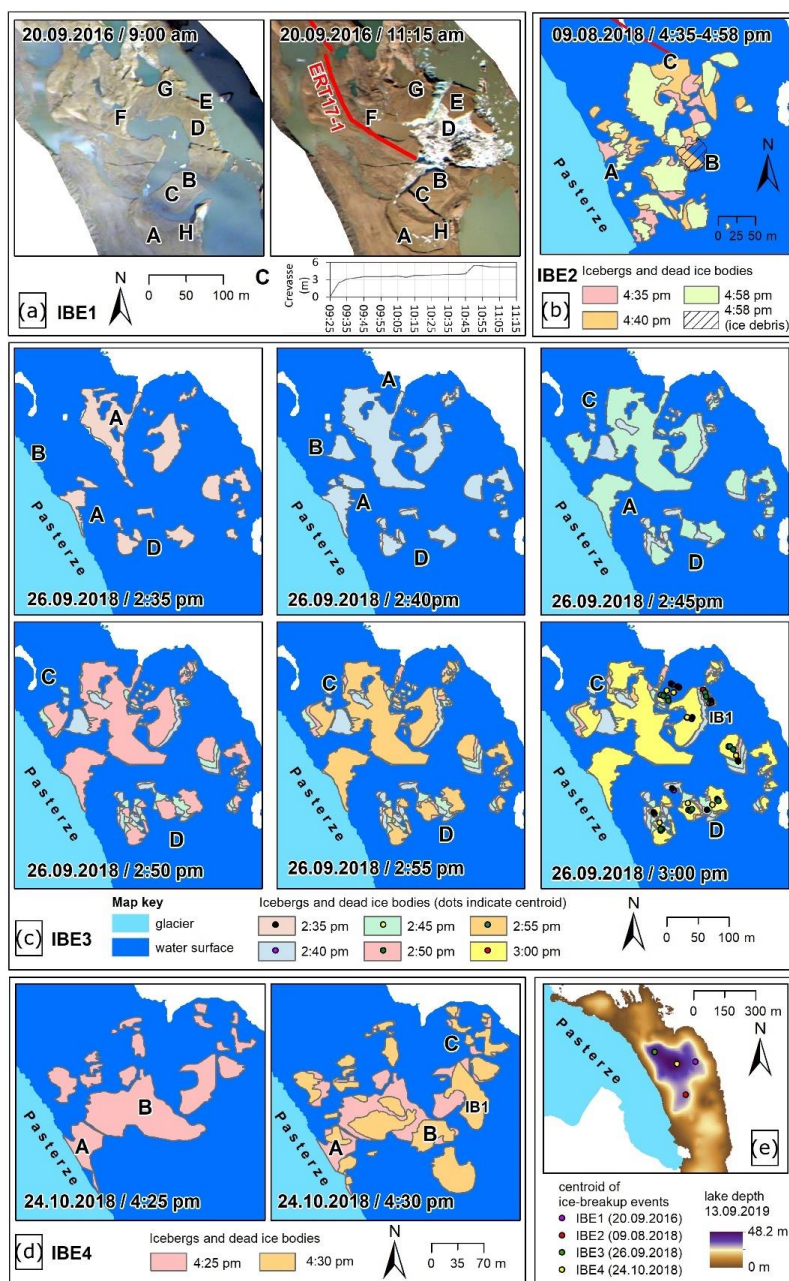
853

854



855

856 **Figure 7:** Land cover evolution in the glacial-proglacial transition zone (0.76 km²) of Pasterze Glacier
 857 between 1998 and 2019 based on visual landform classification. The proglacial basin as defined for
 858 September 2019 is depicted in all maps for comparison. For data sources refer to text and Table 1.
 859 Inset map in (h) depicts a digital elevation model and contour lines (0.5 m interval) of iceberg IB1.

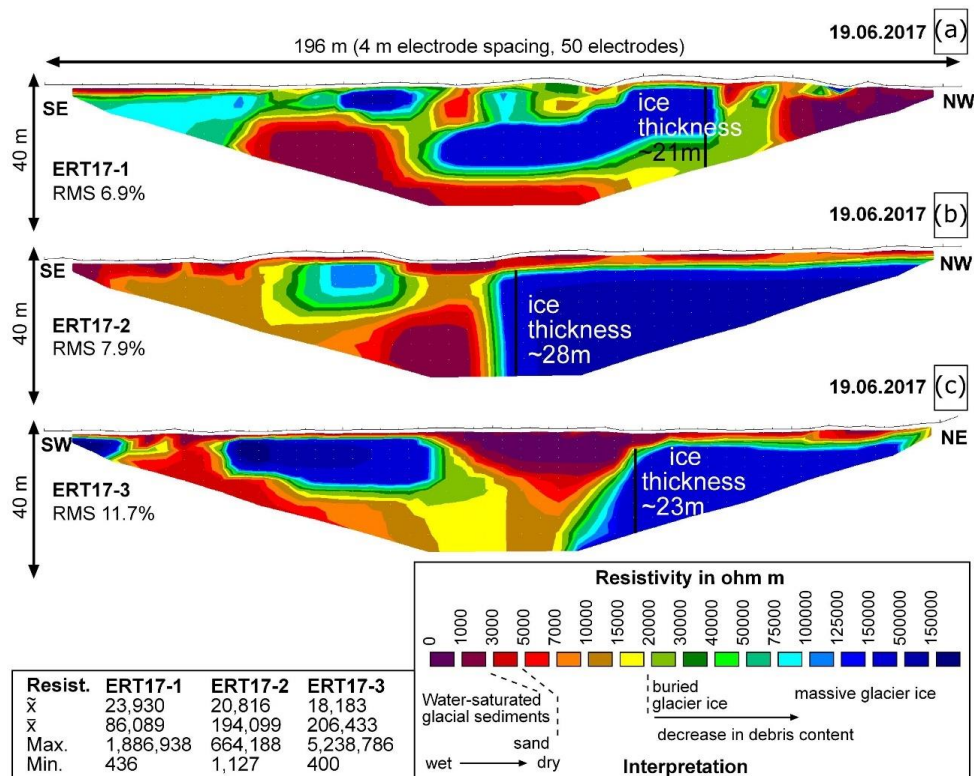


860

861 **Figure 8:** Ice-breakup events (IBE) at the ice-contact lake Pasterzensee monitored by time-lapse
 862 photography: (a) IBE1 20.09.2016; (b) IBE2 09.08.2018; (c) IBE3 26.09.2018; (d) IBE 4 24.10.2018; (e)
 863 overview map of the events. Capital letter in the maps indicate different processes (for details see text).



864



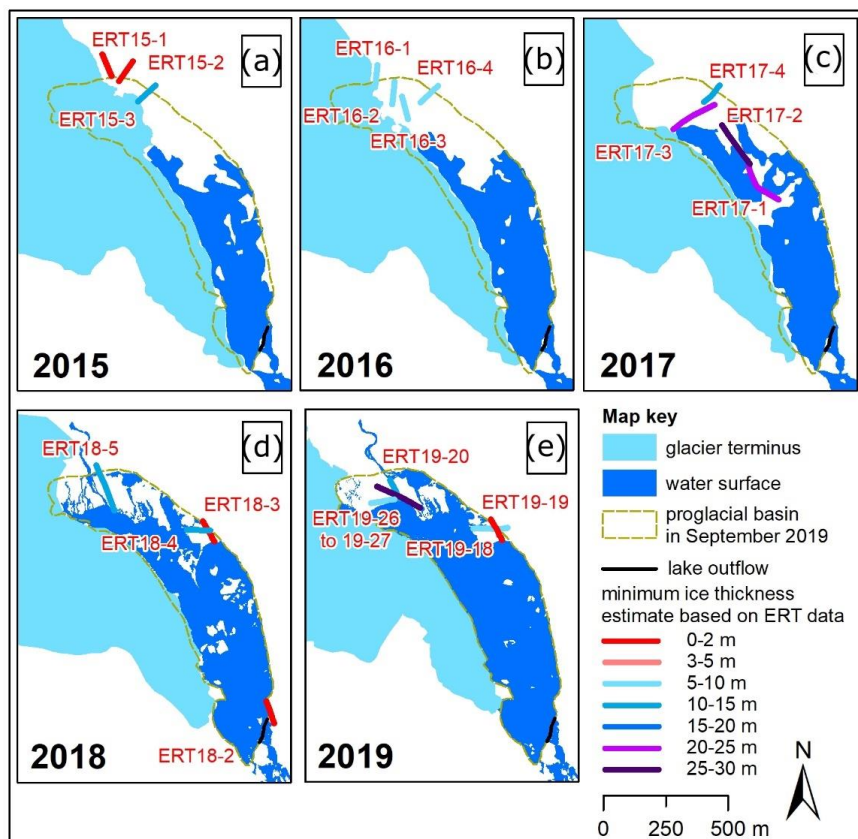
865

866 **Figure 9:** ERT results (Wenner array) and interpretation of three profiles (50 electrodes, 4 m spacing,
 867 length 196 m) measured in the proglacial area of Pasterze Glacier on 19.06.2017 (location: Figs 3, 10).
 868 Summary statistics in the inset table: (a) ERT17-1 – ice lens with a thickness of c.21 m; (b) ERT17-2 –ice
 869 thickness c.28m; (c) ERT17-3 –ice thickness c.23m. For (b) and (c) - ice thickness exceeded the depth of
 870 ERT penetration.

871

872

873



874

875 **Figure 10:** Interpreted minimum ice thicknesses based on electrical resistivity tomography (ERT) data

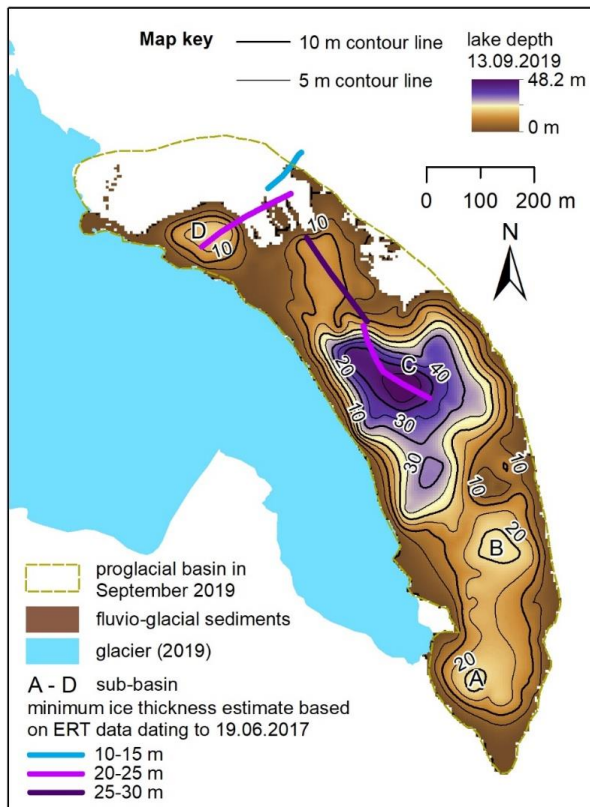
876 (for estimation approach see Fig. 9) in the proglacial area of Pasterze Glacier for (a) 30.09.2015, (b)

877 13.09.2016, (c) 19.06.2017, (d) 13.09.2018, and (e) 09.09.2019 as well as 10.09.2019. “Minimum” means

878 in this case that the base of the ice core was commonly below the depth of ERT penetration.

879

880



881

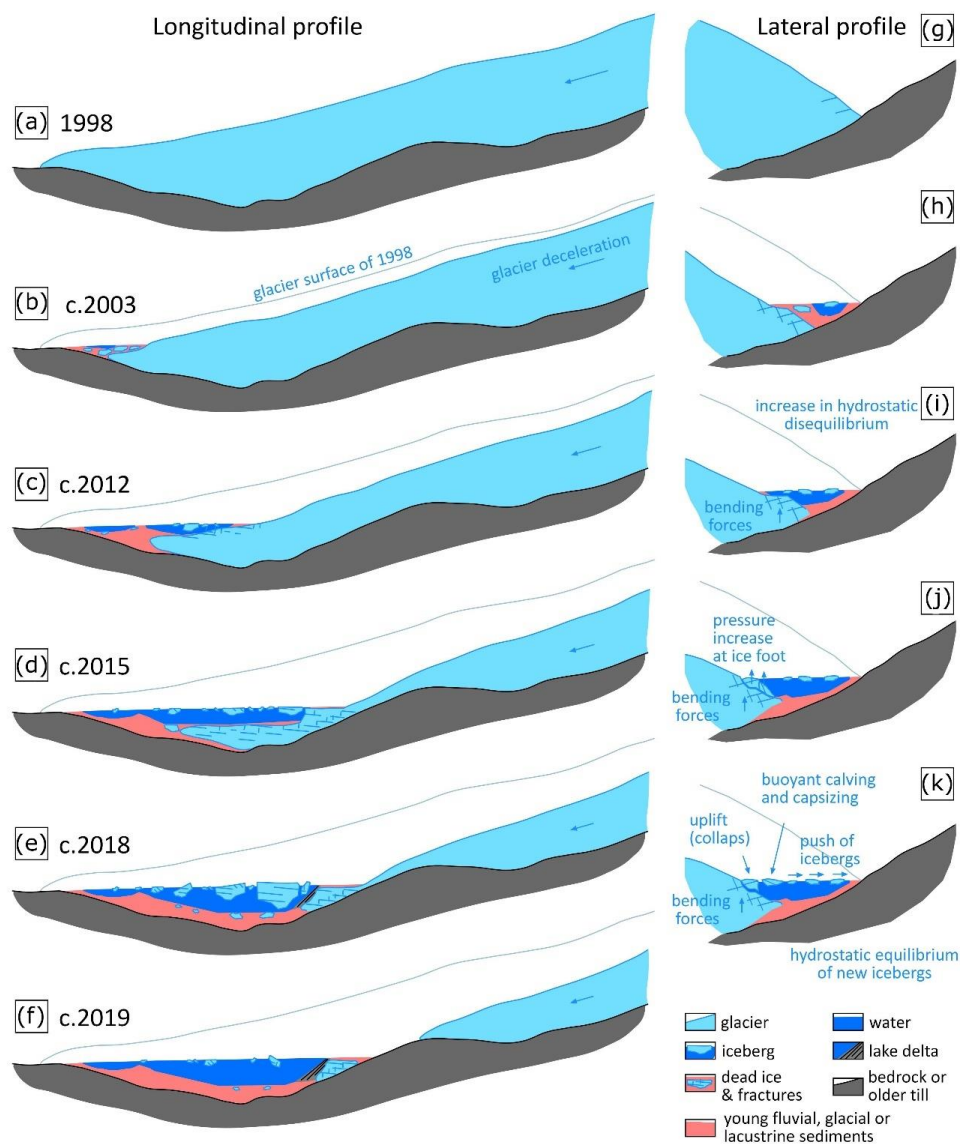
882 **Figure 11:** Lake bathymetry based on echo sounding data acquired in 2019 and its relationship to the

883 ERT data from 2017: glacier extent and lake bathymetry in September 2019 (5 m grid resolution); the

884 extent of the proglacial basin as defined for September 2019 is drawn in the map for orientation.

885

886



887

888 **Figure 12:** Conceptual model of the evolution of the glacial-proglacial transition zone at Pasterze Glacier
 889 since 1998 behind a bedrock threshold: panels (a) to (f) depict changes along a longitudinal profile at the
 890 east side (supraglacial debris-poor) of the glacier tongue; panels (g) to (k) visualize lateral changes and
 891 related processes.

892